J. Fluid Mech. (1998), *vol.* 374, *pp.* 117–144. Printed in the United Kingdom

Excitation and breaking of internal gravity waves by parametric instability

By DOMINIQUE BENIELLI AND JOËL SOMMERIA
Laboratoire de Physique, Ecole Normale Supérieure de Lyon, 46 allée d'Italie, 69 364 Lyon Cedex 07, France

(Received 16 September 1996 and in revised form 3 June 1998)

We study the dynamics of internal gravity waves excited by parametric instability in a stably stratified medium, either at the interface between a water and a kerosene layer, or in brine with a uniform gradient of salinity. The tank has a rectangular section, and is narrow to favour standing waves with motion in the vertical plane. The fluid container undergoes vertical oscillations, and the resulting modulation of the apparent gravity excites the internal waves by parametric instability.

Each internal wave mode is amplified for an excitation frequency close to twice its natural frequency, when the excitation amplitude is sufficient to overcome viscous damping (these conditions define an 'instability tongue' in the parameter space frequency-amplitude). In the interfacial case, each mode is well separated from the others in frequency, and behaves like a simple pendulum. The case of a continuous stratification is more complex as different modes have overlapping instability tongues. In both cases, the growth rates and saturation amplitudes behave as predicted by the theory of parametric instability for an oscillator. However, complex friction effects are observed, probably owing to the development of boundary-layer instabilities.

In the uniformly stratified case, the excited standing wave is unstable via a secondary parametric instability: a wave packet with small wavelength and half the primary wave frequency develops in the vertical plane. This energy transfer toward a smaller scale increases the maximum slope of the iso-density surfaces, leading to local turning and rapid growth of three-dimensional instabilities and wave breaking. These results illustrate earlier stability analyses and numerical studies. The combined effect of the primary excitation mechanism and wave breaking leads to a remarkable intermittent behaviour, with successive phases of growth and decay for the primary wave over long timescales.

1. Introduction

Parametric instability is a general mechanism of excitation for an oscillator, owing to a modulation of its natural frequency. The case of a simple pendulum will be briefly discussed in §3, as an introduction to the subject. The case of surface waves, excited by a vertical oscillation of the container, has been the subject of considerable interest (e.g. the review by Miles & Henderson 1990). Each spatial mode behaves like an oscillator, and the modulation of its natural frequency results from the apparent gravity due to the container acceleration. While the first observations trace back to Faraday (1831), the subject has been recently revived as providing examples of pattern formation in nonlinear systems.

By comparison, internal waves have rarely been considered. Interfacial waves propagate at the interface between a heavy fluid and an upper, lighter fluid. Their

dynamics is similar in many respects to surface waves. Their excitation by parametric instability has been studied theoretically by Sekerzh-Zen'kovitch (1983*a*) and experimentally by Kalinichenko (1986) and Kalinichenko, Sekerzh-Zen'kovitch & Timofeev (1991). We reproduce similar experiments as a reference case in §4, with their theoretical interpretation.

Our main purpose is to investigate the case of a continuously stratified fluid (§5). The wave excitation by a modulation of the apparent gravity has been theoretically considered in this case by Sekerzh-Zen'kovitch (1983*b*), but not realized previously in a laboratory experiment. While interfacial waves propagate only horizontally, internal waves in the uniformly stratified case can propagate at any angle to the horizontal, and the dispersion relationship is quite different from interfacial waves: the wave frequency depends on the angle of the wave vector with the horizontal, but not on the wavelength. Therefore, the parametric instability, which dominantly excites waves at a frequency of half the excitation frequency, does not select a given wavelength, in contrast to the interfacial (or free-surface) case. This is an interesting physical property, as instability processes usually select the most amplified wavelength. Furthermore, this method of internal wave production does not specify a wave geometry, unlike usual wavemakers. It is therefore appropriate to generate and investigate random wave fields, and some internal wave turbulence with universal k^{-3} energy spectra has been generated with this method by Benielli & Sommeria (1996). In a different tank geometry, the same mechanism of wave generation has been used to observe a wave attractor (Maas *et al.* 1997).

In this context, a careful investigation of internal wave generation by a modulation of the apparent gravity is useful, and this is the main goal of the present paper. We first analyse the initial growth of the parametric instability (§5.3), and discuss the problem of mode selection. The nonlinear saturation of the parametric instability is then analysed in §5.4. We show that the saturation of the instability is partly due to a phase shift of the wave with respect to the forcing, as in a usual pendulum. However, a second mechanism simultaneously occurs, specific to the continuously stratified internal waves: the primary wave is observed to be unstable, exciting secondary waves by another form of parametric instability, leading to wave-breaking and turbulence by subsequent instabilities (§6). As a result of these secondary instabilities, the parametrically excited primary wave never reaches a steady state, by contrast with the interfacial case, and intermittence is observed, corresponding to a succession of wave amplification and decay by breaking.

Such a parametric instability of the primary wave commonly occurs in a continuously stratified fluid: a secondary wave is excited by the periodic tilt induced by the primary wave. The secondary wave has a frequency of half the primary wave and a smaller wavelength. The parametric instability is therefore an important mechanism of energy transfer from the primary wave to smaller wavelengths. Its linear regime has been studied by Floquet analysis in the case of a propagating plane wave (Mied 1976; Drazin 1977; Klostermeyer 1991; Lombard & Riley 1996). The case of a standing wave has been discussed by McEwan (1971) and McEwan & Robinson (1975). These authors also performed laboratory experiments showing that the subharmonic instability initiates small-scale disturbances or 'traumata', leading to local density overturning and mixing. They reproduced this instability in a uniformly stratified fluid contained within a cylinder rotating with an oscillating motion, to simulate conditions occurring locally in an internal wave. Thorpe (1994) observed a parametric instability in a different configuration, with a primary wave produced in an oscillating tilted tube.

The subharmonic nature of the internal wave instability has been observed in these

experiments, but the description remained qualitative. A more detailed analysis has been made possible in direct numerical simulations by Bouruet-Aubertot, Sommeria & Staquet (1995, 1996). In particular, the instability was shown to organize in a wave packet, with growth rate in agreement with the linear stability analysis. Subsequent instabilities rapidly lead to wave breaking, feeding a form of stratified turbulence with k^{-3} energy spectra. We observe similar secondary wave packets in the present experiments (§6), as well as k^{-3} energy spectra when turbulence has developed (Benielli & Sommeria 1996).

The parametric instability is a particular form of resonant triad interactions, occurring in the oceanic thermocline, where internal waves are excited at fairly high frequency and long wavelengths (by surface waves), and feed a continuous spectrum of lower frequencies and higher wavenumbers by resonant interactions (e.g. Muller *et al.* 1986). This cascade process leads to sporadic wave breaking, with production of turbulence and mixing. Klostermeyer (1991) argued that parametric instability may be an important process in the atmospheric thermosphere, explaining, for instance, the acoustic double peaks commonly found in high-frequency Doppler spectra near thunderstorms.

Therefore, parametric instabilities seem ubiquitous in continuously stratified fluids, although their role in generating turbulence is far from clear. We study here a more controlled case, excitation of a wave by a modulation of the apparent gravity, which may shed some light on the mechanisms of instability of an internal wave into secondary waves. In particular the intermittent behaviour over long timescales may be of general relevance.

2. Experimental apparatus and procedure

The continuous stratification is produced by salt concentration in a Plexiglas water tank (figure 1(*a*)) with a rectangular (nearly square) vertical section. The tank is narrow, 9.6 cm wide × 26.1 cm long (filled with water to a height of 25 cm), to excite mostly modes of internal waves in a vertical plane. The tank is slowly filled from the bottom by water with increasing salt concentration, prepared by the computer programmed displacement of pistons in two cylinders, one filled with pure water and the other with concentrated salt, as sketched in figure 1(*b*). The salt is sodium nitrate, which has the advantage of being highly soluble, with only a weak modification of water viscosity (increase of the kinematics viscosity by 4% for a density 1.1). This allows fairly high density differences (10%) to be produced, which is useful for sustaining relatively high wave frequencies.

To study interfacial waves, we fill the tank with water (coloured with fluorescein) up to half height (12.5 cm), and then add kerosene up to 25 cm. The density of water is $\rho_1 = 1.00\ \mathrm{g\ m^{-1}}$ while the density of kerosene is $\rho_2 = 0.79\ \mathrm{g\ ml^{-1}}$. The respective viscosities are $\nu_1 = 1.0 \times 10^{-6}\ \mathrm{m^2\ s^{-1}}$ and $\nu_2 = 1.6 \times 10^{-6}\ \mathrm{m^2\ s^{-1}}$.

The tank is mounted on a platform with an oscillating motion of vertical translation, driven by a crank and a motor, as sketched in figure 1(*a*). The amplitude of oscillation is mechanically adjusted by a screw on the crank (in the range 0–120 mm, with precision 0.5 mm). The frequency of oscillation f_e is set by the motor speed with a good precision (better than 10^{-3}), which is necessary to get a reproducible wave excitation. A video camera is mounted on the platform to monitor the fluid motion in the oscillating frame of reference.

The wave field in the continuously stratified case is visualized by the displacement of dye bands. These are initially produced by periodic injection of fluorescein in the filling

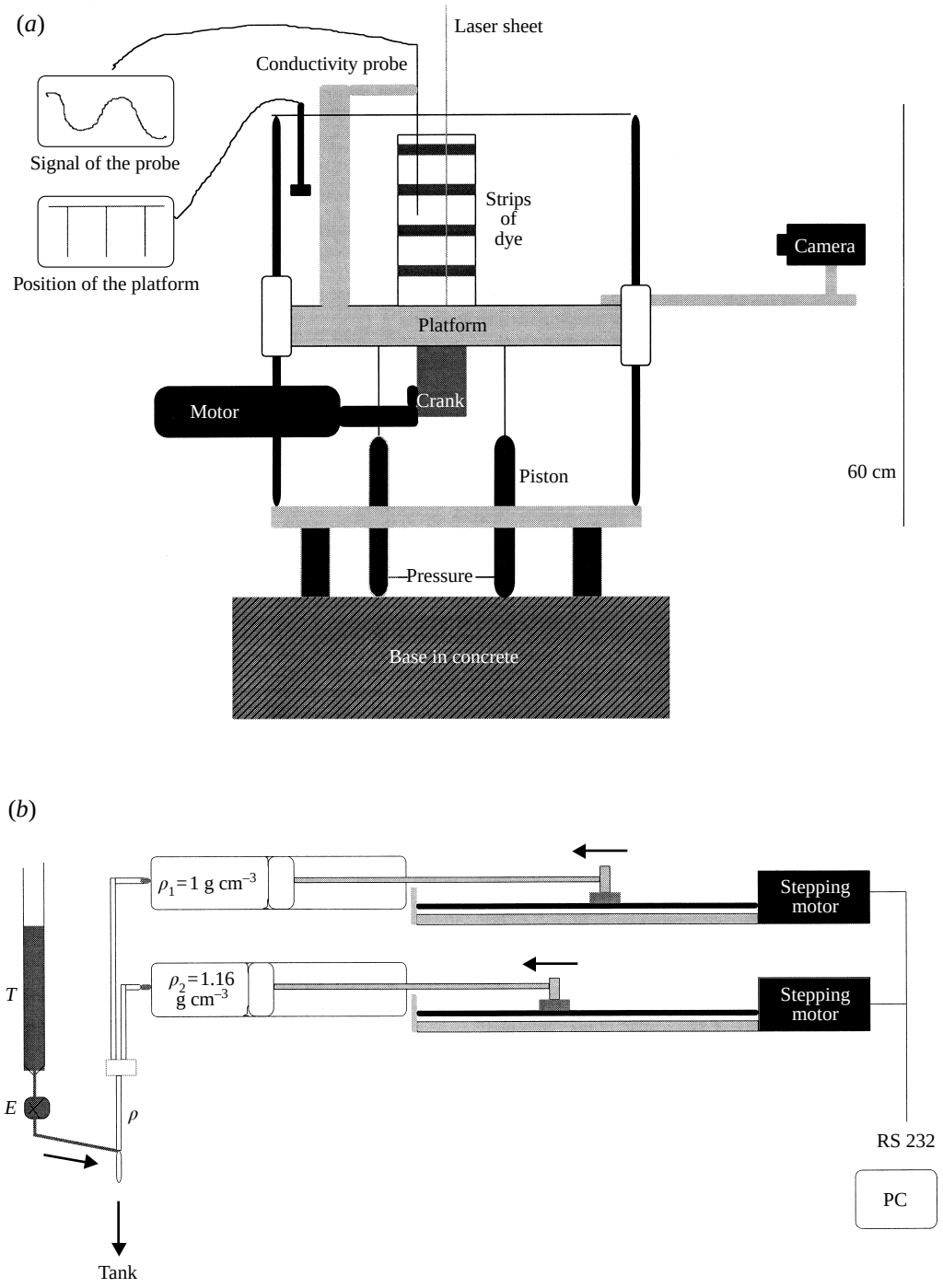

FIGURE 1. (*a*) Sketch of the experimental apparatus. The tank filled with stratified fluid is fixed onto the oscillating platform. The motor drives the platform with a sinusoidal vertical motion through a crank. The pressure in the piston balances the platform weight. The conductivity signal is recorded, as well as peaks marking the high position of the platform (through an electrical contact). (*b*) Filling system to prepare any vertical density profile with two computer programmed pistons, pushing pure water (with density $\rho_1 = 1$ g ml^{-1}) and salt water (with density $\rho_2 = 1.16$ g ml^{-1}), respectively, mixed in a solution with a resulting density ρ; dye in the reservoir T is periodically injected through an electrovalve E to produce dye strips.

brine entering the tank bottom, marking the fluid parcels with a given density. The deformation of the resulting dye strips is visualized by the fluorescence excited by a vertical laser sheet. The amplitude and phase of a simple primary wave (as shown in figure 8) can be obtained by measuring the maximum vertical displacement of these strips, using image processing. However, we are not able to quantitatively analyse more complex wave fields by this method, and we use instead a conductivity probe.

Time series of the local density are obtained by this conductivity probe, which can be positioned at different depths. It is a four-electrode probe (Precision Measurement, model 5201), which has a spatial resolution 0.5 mm. The probe is used with the associated electronic device from the same company. An a.c. current at 80 kHz is introduced by two electrodes, and the corresponding potential difference measured by two different electrodes to avoid the effect of contact resistance. The potential difference is treated by a lockin amplifier (in the same box), leading to a relative precision on conductivity of about 1%. The output signal from this electronic device is introduced in a 16 bit A/D acquisition board, and processed in a PC computer. The phase of the platform oscillating is recorded simultaneously with the probe signal, by measuring the potential difference across an electric contact, closing a circuit (fed by a DC power supply) when the platform is up; the signal of the platform displacement $\cos \omega_e t$ is then reconstructed.

We perform various processing operations on the signal. In particular we filter the density signal $\rho'(t)$ around the primary wave frequency $\frac{1}{2}\omega_e$, extracting the oscillating $\rho_p(t)$ in the primary wave component (we use a Blackman filter band pass 0.02 Hz). We consider that this primary wave has a slowly varying amplitude $A(t)$ and phase $\phi(t)$, $\rho_p(t) = A(t)\cos(\frac{1}{2}\omega_e t + \phi(t))$. We experimentally determine these quantities by

$$\left.\begin{aligned} A(t) &= \langle \rho_p(t)^2 \rangle^{1/2}, \\ \cos\phi(t) &= 2\langle \rho_p(t)\cos\omega_e t/2 \rangle / \langle \rho'(t)^2 \rangle^{1/2}, \\ \sin\phi(t) &= -2\langle \rho_p(t)\sin\omega_e t/2 \rangle / \langle \rho'(t)^2 \rangle^{1/2}, \end{aligned}\right\} \tag{2.1}$$

where $\langle \cdot \rangle$ is a sliding average, calculated over a sufficient number of periods, but shorter than the typical time for the instability evolution (we use a Blackman low-pass filter with band pass 0.02 Hz).

During the growth of a simple primary wave, we compared this amplitude and phase with the vertical displacement obtained from image analysis (we expect that $\rho' = \eta \mathrm{d}\tilde{\rho}/\mathrm{d}z$), where $\tilde{\rho}(z)$ is the basic vertical density profile, initially prepared when the tank is filled. We find an excellent agreement for amplitude, but we observe phase lags: the wake of the probe itself generates an internal wave, which somewhat perturbs the probe measurements.

3. The pendulum as a general model of parametric instability

To interpret our experimental results, it is first useful to consider a simple pendulum with natural frequency $\omega = (g/l)^{1/2}$, whose suspension point vertically oscillates with amplitude Z_0 and frequency ω_e, so the apparent gravity is $g + Z_0\omega_e^2 \cos\omega_e t$. The angular displacement ζ therefore satisfies

$$\ddot{\zeta} + 2Q\dot{\zeta} + \omega^2[1 + F\cos(\omega_e t)]\sin\zeta = 0, \tag{3.1}$$

where the excitation parameter

$$F \equiv Z_0\omega_e^2/g, \tag{3.2}$$

has been introduced, as well as a friction coefficient Q.

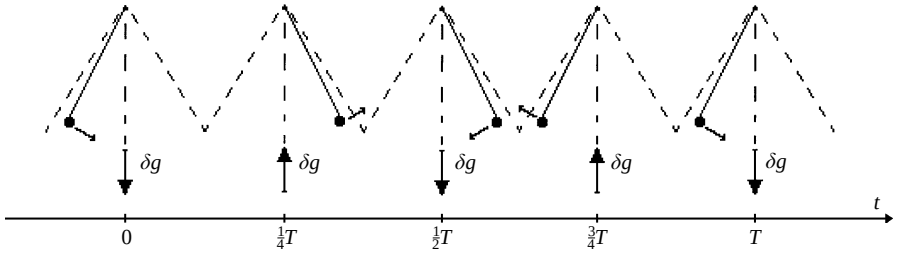

FIGURE 2. The mechanism of parametric instability illustrated by a sketch of a pendulum at successive phases with the corresponding modulation δg of the apparent gravity (the extremal positions of the pendulum are indicated by dashed lines and its velocity by the arrow). The apparent gravity is stronger than average when the pendulum moves downward and is weaker than average when the pendulum moves upward. This is possible when the excitation period is half T, the natural period of the pendulum.

The instability mechanism is easily understood by the following arguments. When the pendulum moves downward, the apparent gravity (in the reference frame of the suspension point) is higher than average, as shown in figure 2 ($t = 0$). Therefore, it is pushed downward more strongly. When the pendulum moves upward (figure 2, $t = \frac{1}{4}T$), the apparent gravity is lower than average. The oscillation is globally amplified by this mechanism, which is possible when the gravity oscillates by one period during half a pendulum period, i.e. $\omega_e \approx 2\omega$, as shown in figure 2 (there are other frequencies of instability, with $\omega_e/\omega = 2/n$, for any integer n, but with much higher thresholds, so we do not consider them). Furthermore, appropriate phase relationship must be satisfied between the excitation and the pendulum oscillation. This condition can be precisely stated by averaging the equation for energy (obtained by multiplying (3.1) by $\dot{\zeta}$) over one period. Introducing the slowly varying complex amplitude $A(t) = |A|(t)\exp(\mathrm{i}\,\phi(t))$ by

$$\zeta(t) = \mathrm{Re}\,[A(t)\exp(\mathrm{i}\omega_e t/2)], \tag{3.3}$$

we then get the growth rate

$$\mathrm{d}\,|A|/|A|\,\mathrm{d}t = s\sin(2\phi) - Q, \quad \text{with} \quad s = \omega_e F/8. \tag{3.4}$$

The growth is maximum for $\phi = \frac{1}{4}\pi$, and a maximal decay occurs for $\phi = -\frac{1}{4}\pi$.

The phase is obtained by a redefined analysis, using a multiscale expansion (e.g. Nayfeh 1973)

$$\frac{\mathrm{d}\phi}{\omega\,\mathrm{d}t} = \Delta + \tfrac{1}{4}F\cos 2\phi - \tfrac{1}{4}|A|^2, \tag{3.5}$$

where $\Delta = \omega - \frac{1}{2}\omega_e$ is the frequency misfit. Instability is then shown to occur within an instability tongue in the parameter space (ω_e, F), defined by the range (represented in figure 5)

$$-(s^2 - Q^2)^{1/2} < \Delta < (s^2 - Q^2)^{1/2}. \tag{3.6}$$

The tongue extremity is the minimum instability threshold $s = Q$, occurring with $\Delta = 0$. At sufficiently large forcing (far from the tip), the width of the tongue given by (3.6) is just $2s = \frac{1}{4}F\omega_e$.

For a harmonic oscillator, the exponential growth would persist without bound. However, for a pendulum, the period increases with amplitude, corresponding to the phase shift indicated by the last term in (3.5). The resulting growth rate (3.4) is reduced

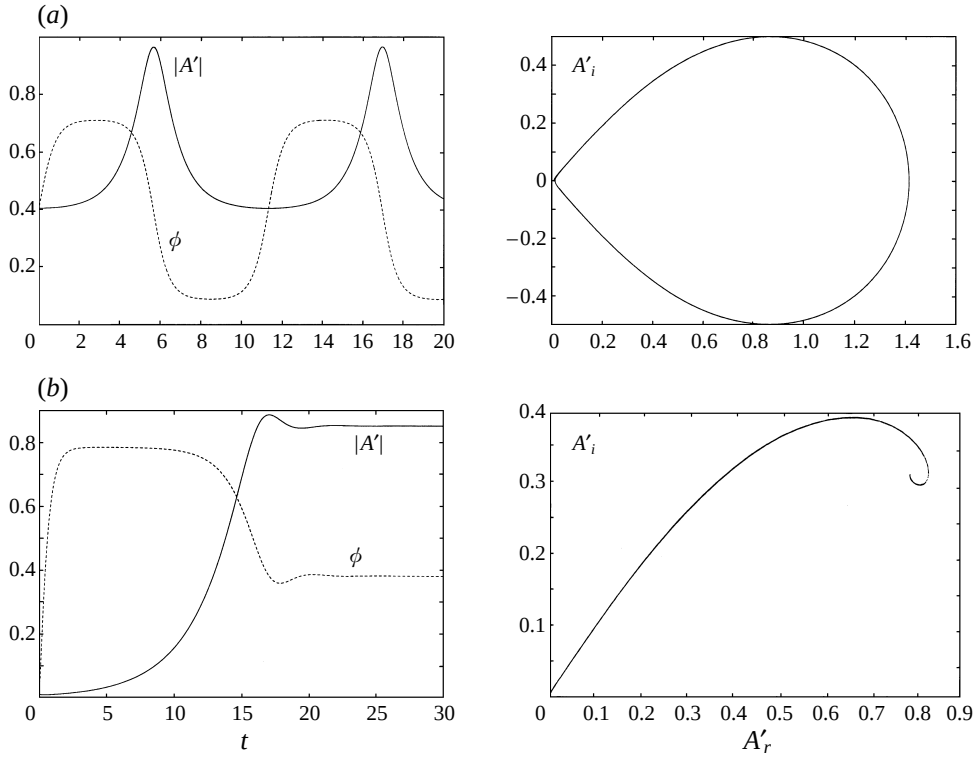

FIGURE 3. Numerical solution of the amplitude equation (3.7). Amplitude and phase ϕ versus time (left-hand side), and trajectories in the phase space (right-hand side). The reduced complex amplitude $A' = (\omega/4s)^{1/2} A$ is represented. The excitation is exactly at the frequency of the parametric resonance ($\Delta = 0$). (*a*) No dissipation $Q/s = 0$. A periodic modulation of the amplitude is obtained. After an exponential growth with phase $\phi = \frac{1}{4}\pi$, the nonlinear effects produce a phase shift resulting in a decay with phase $\phi = -\frac{1}{4}\pi$. The period of modulation depends on the initial perturbation. The phase space trajectory seen on the right-hand side is a homoclinic cycle corresponding to the unstable fixed point $(A_r, A_i) = (0, 0)$. (*b*) $Q/s = 0.69$. The amplitude modulation is damped and a stable fixed point with a permanent oscillation amplitude is reached.

until saturation occurs. The two evolution equations (3.4) and (3.5) can be combined into an equation for the complex amplitude A

$$\dot{A} = (-Q + \mathrm{i}\Delta)\, A + \mathrm{i}s\bar{A} - \mathrm{i}\tfrac{1}{4}\omega\, \bar{A}A^2. \tag{3.7}$$

The form of this equation can be deduced from general symmetry arguments (Thual, Douady & Fauve 1989), so we expect it to describe many other cases of parametric instability, for instance with surface and internal waves.

Typical (numerical) solutions of (3.7) are plotted in figure 3. Inside the instability tongue (3.6), the system (3.7) tends to the stable fixed point

$$|A|^2 = \frac{4}{\omega}(\Delta + (s^2 - Q^2)^{1/2}) \quad \left\{ \begin{array}{c} \sin(2\phi) = Q/s \\ \cos(2\phi) > 0 \end{array} \right\}, \tag{3.8}$$

which determines the phase and amplitude of the permanent oscillation (there are in fact two possible phases, differing by π). For a small dissipation parameter Q/s, amplitude and phase oscillate before reaching this permanent regime (see figure 3(*a*)), but this oscillation is damped as the dissipation Q/s is close to 1 (figure 3(*b*)).

When Δ is progressively increased from negative values, so that the instability tongue is crossed with decreasing excitation frequency, the permanent regime amplitude progressively increases from the threshold $\Delta = -(s^2-Q^2)^{1/2}$: the tongue edge with negative Δ corresponds to a supercritical bifurcation. For $\Delta > (s^2-Q^2)^{1/2}$, the amplitude still grows, but this solution coexists with the state of rest, which is also stable. If by contrast the instability tongue is crossed with increasing frequency, instability appears for $\delta = (s^2-Q^2)^{1/2}$, and the system directly reaches the amplitude (3.8), so that hysteresis is expected; the tongue edge with positive Δ corresponds to a subcritical bifurcation.

When several coupled oscillators are present, their instability tongues can overlap. The amplitude equation is then more complex than (3.7), involving coupling between the amplitudes of the different oscillators (see Meron 1987).

The oscillations of a confined continuous media can be generally analysed as a set of eigenmodes. Each of these eigenmodes behaves as an oscillator and can be parametrically excited like a pendulum. If the frequencies of these eigenmodes are well separated (and not in rational ratio), their interactions can be neglected in the weakly nonlinear regime. Each mode interacts with its harmonics, resulting in a change to its natural frequency, and a saturation of the parametric instability, as for the pendulum. The normal form (3.7) is obtained and justified from general symmetry of the parametric instability (Thual *et al.* 1989). The determination of the coefficients from fluid dynamics depends on the particular problem.

The case of surface waves has been treated by Miles (1984), and the case of waves at the interface between two deep fluids by Sekerzh-Zen'kovich (1983*a*). The result of Sekerzh-Zen'kovich (1983*a*) can be identified with (3.7) by the following correspondence between the amplitude $|A|$ and the maximum vertical interface displacement η_m, scaled by the wavelength λ,

$$|A| = \sqrt{2}\pi \frac{(\rho_1^2+\rho_2^2)^{1/2}}{\rho_1+\rho_2} \frac{\eta_m}{\lambda}. \tag{3.9}$$

In particular, the wave frequency decreases with amplitude as in a pendulum.

For the continuously stratified case (with the Boussinesq approximation) Sekerzh-Zen'kovich (1983*b*) similarly found results leading to the following correspondence:

$$|A| = \frac{q_z \eta_m}{\sqrt{8}} = \frac{\pi \eta_m}{\sqrt{2}\lambda_z}, \tag{3.10}$$

where η_m is the maximum vertical particle displacement with respect to their positions at rest, and $\lambda_z = 2\pi/q_z$ the wavelength in the vertical direction. An isolated mode is assumed to grow at leading order, which is not truly justified owing to the overlap of the instability tongues, but has the advantage of yielding again the pendulum equation (3.7) for the equivalent amplitude (3.10).

4. Parametric instability of interfacial waves

At certain frequencies of the oscillating platform, we observe the formation of standing waves of considerable amplitude at the liquid interface. The frequency of these internal waves is found to be half the excitation frequency f_e, as expected for parametric instability. Note that the (upper) free surface remains unperturbed in the frequency range that we explore.

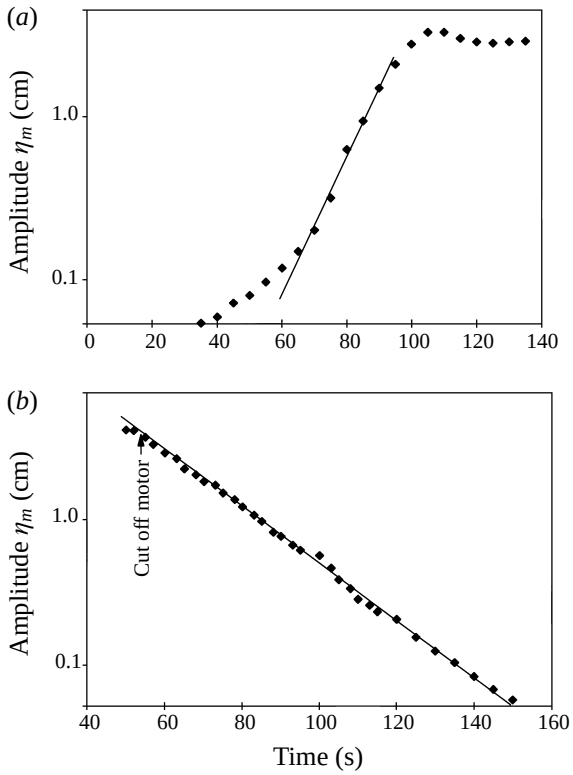

FIGURE 4. Amplitude η_m of the interfacial wave versus time (mode $n = 1$), obtained as the successive elevation maxima of the interface, measured on video records (the precision is about 0.5 mm). (*a*) Growth at excitation frequency 1.108 Hz ($\Delta \approx 0$), with amplitude $Z_0 = 3.5$ cm, beginning at $t = 0$. The theoretical growth $\exp(s-Q)\,t$ is indicated by the straight line ($s = 0.150\ \mathrm{s}^{-1}$ is given by (3.4) and $Q = 0.046\ \mathrm{s}^{-1}$ from the measured decay, see (*b*)). (*b*) Decay after turning off the excitation, by stopping the motor of the oscillating platform (the time origin of the graph is arbitrary); the best fit by an exponential, $\exp(-Qt)$ with $Q = 0.046\ \mathrm{s}^{-1}$, is represented by the straight line.

We restrict the theoretical description to interfacial waves with fairly large wavelength (> 10 cm), so that various effects are limited to thin boundary layers. Therefore we first consider the inviscid modes, containing integer numbers (n, m) of half wavelengths over the length L and width W of the tank, respectively. For simplicity, we choose to select one of the first two-dimensional modes ($n = 1$ or 2, $m = 0$), by an appropriate choice of the range of the excitation frequency f_e. The total fluid height is denoted by H, while each fluid layer has the same depth $\frac{1}{2}H$. In the case of the narrow tank that we use here, three-dimensional modes have a well separated frequency and are not excited. The natural frequency is then given by the textbook formula (e.g. Lamb 1932, §231),

$$\omega(q)^2 = \frac{qth(\frac{1}{2}qH)}{(\rho_1+\rho_2)}[(\rho_1-\rho_2)\,g+\gamma q^2], \quad q = \frac{n\pi}{L}, \tag{4.1}$$

In fact, we are close to a condition of deep water $th(\frac{1}{2}qH) \approx 1$. We have estimated the coefficient of surface tension $\gamma = 20 \times 10^{-3}\ \mathrm{J\ m^{-2}}$ from observations of the meniscus. The corresponding correction on frequency is 0.07% for $n = 1$, and 0.3% for $n = 2$, and we shall neglect it.

Mode number n	1	2
Q_{calc} (s^{-1})	3.1×10^{-2}	4.2×10^{-2}
Q (s^{-1})	4.6×10^{-2}	7.3×10^{-2}

TABLE 1. Decay rate Q_{calc} for interfacial waves calculated from (4.2) compared to the measured rate Q.

The influence of the small viscous effects can be calculated by a boundary-layer approximation. Harrison (1908) has shown that a viscous reduction of frequency $\Delta\omega \approx (\frac{1}{2}\omega\nu)^{1/2}\frac{1}{2}\zeta$ should occur (see also Thorpe 1968). This reduction is only 0.2% for $n=1$, and 0.3% for $n=2$, so we neglect it. The main effect of viscosity is a wave damping that we obtain by a boundary-layer approximation (e.g. Lamb 1932, §329). We calculate the laminar boundary-layer structure at the solid walls, matched with the inviscid solution in the bulk. The energy dissipated over one wave period in these boundary layers is then calculated, and the rate of energy decay is obtained by dividing this dissipation by the total wave energy. The corresponding decay rate Q_{bound} for amplitude is then half this energy decay rate. Another contribution Q_{inter} to the decay rate is similarly introduced by the boundary layer occurring at the interface between the two fluids. The total decay rate is then $Q_{calc}=Q_{bound}+Q_{inter}$ (there is also a contribution by shear effects in the bulk, but it is quite negligible in our case). We find

$$\left.\begin{aligned} Q_{bound} &= \frac{\rho_1(\frac{1}{2}\omega\nu_1)^{1/2}+\rho_2(\frac{1}{2}\omega\nu_2)^{1/2}}{\rho_1+\rho_2}\left[\frac{q}{\operatorname{sh} qH}\left(1-\frac{H}{L}\right)+\frac{1}{W}+\frac{1}{L}\right], \\ Q_{inter} &= \left(\frac{\rho_1(\frac{1}{2}\omega\nu_1)^{1/2}}{[1+(\rho_1/\rho_2)(\nu_1/\nu_2)^{1/2}]^2}+\frac{\rho_2(\frac{1}{2}\omega\nu_2)^{1/2}}{[1+(\rho_2/\rho_1)(\nu_2/\nu_1)^{1/2}]^2}\right)\frac{4q\cosh^2(\frac{1}{2}qH)}{(\rho_1+\rho_2)\sinh qH}. \end{aligned}\right\} \tag{4.2}$$

In the limit of deep water $qH \gg 1$, and for $\rho_1 \approx \rho_2$, $\nu_1=\nu_2\equiv\nu$, (4.2) reduces to the approximation $Q_{calc}\approx(\frac{1}{2}\omega\nu)^{1/2}(1/W+1/L+\frac{1}{2}k)$ used by Thorpe (1968).

We have compared the result (4.2) with the measured rate of free decay of the wave. For that purpose we run the experiment with appropriate conditions for wave excitation by parametric instability (see below), and stop the tank motion before the wave has grown to a large amplitude. We then obtain the decay rate by measuring on a video record the maximum vertical displacement at each wave period, as shown in figure 4(*b*). The measured dissipation rates Q appear to be significantly stronger than theory, see table 1. The discrepancy increases with mode number, and may be associated with hysteresis in wetting effects on the wall, as discussed by Miles (1967) for surface waves.

In order to study the parametric instability, experiments with different excitation frequency f_e and amplitude Z_0 are performed. In practice, we manually set an amplitude Z_0, turn on the driving motor at a low frequency, and then increase the frequency, by small steps (0.5×10^{-2} Hz) when approaching the instability tongue of the mode under study. We thus move along a line in the (f_e, F) space, as marked by dots and crosses in figure 5. We draw a dot when instability is not observed (after a waiting time about 20 min), and a cross when instability grows, so that the left-hand side of the instability tongue is detected. To obtain the right-hand side of the tongues, we set a higher exciting frequency well beyond the instability tongue, and progressively decrease this frequency. The observed tongue is centred around a frequency very close to the theoretical one (4.1), although slightly higher (1 or 2%). The width of the tongue

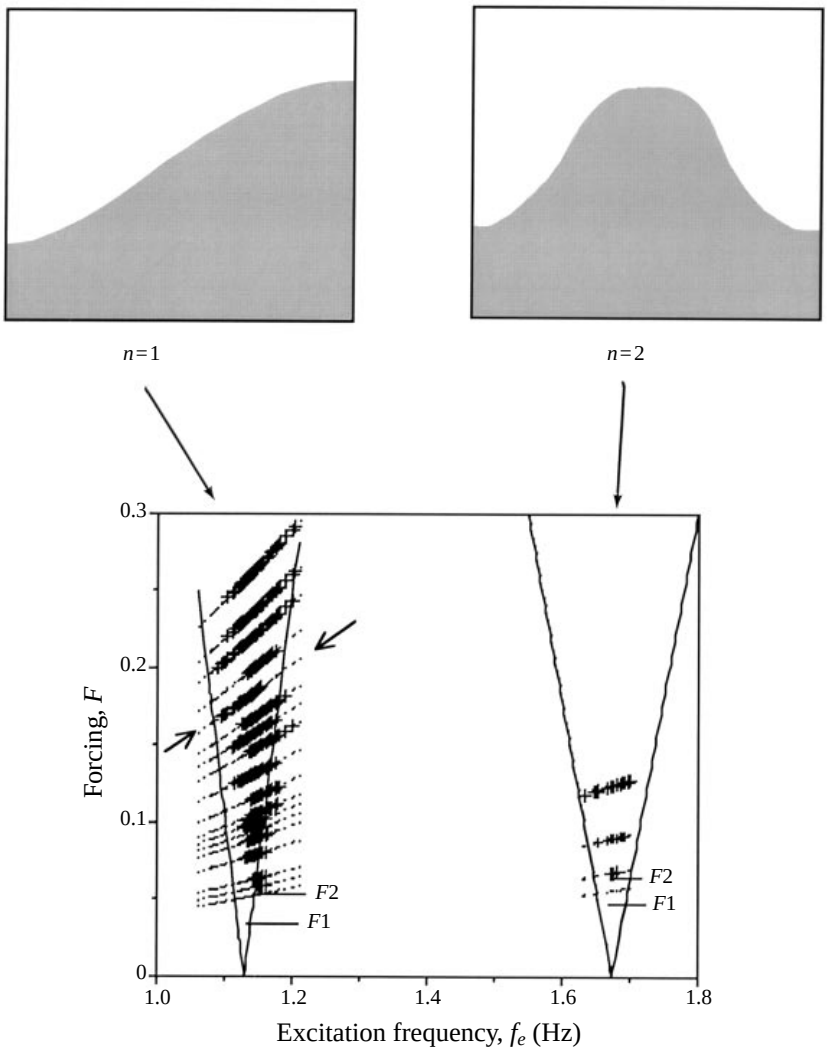

FIGURE 5. Instability diagram for the interfacial modes $n = 1$ (left) and $n = 2$ (right). The excitation frequency f_e is in the abscissa and the forcing parameter F in the ordinates. The sign (+) denotes an observed instability, the sign (.) the absence of instability. The theoretical instability tongues (in the absence of dissipation) are given by the solid lines. The theoretical threshold amplitudes, resulting from the boundary-layer approximation (4.2) are represented by $F1$, and the threshold calculated from the measured decay rate Q is indicated by $F2$. The arrows indicate the path followed in figure 6.

is also in good agreement with theory, although some fluctuations in the threshold position are observed.

While the position and width (at large enough F) of the instability tongue depend only on the natural frequency of the mode, the ordinate of the tip is proportional to the friction rate, corresponding to $s = Q$ from (3.6). The experimental threshold is higher than this prediction obtained from the theoretical friction Q_{calc}, labelled as $F1$. The observed threshold is, however, in good agreement with the value $s = Q$ predicted from the measured friction, labelled as $F2$ in figure 5.

We have checked also the growth rate of the instability. A typical result is

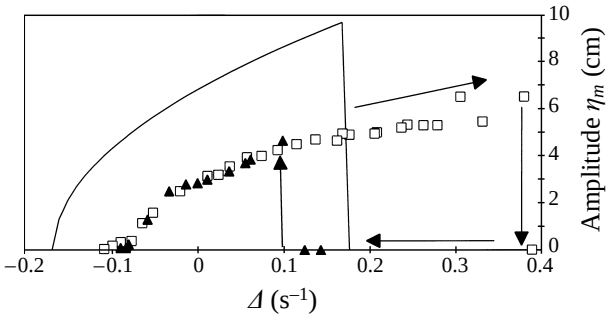

FIGURE 6. Amplitude η_m of the mode $n = 1$ in the permanent regime (interfacial wave) as a function of the frequency misfit Δ, following the path shown in figure 5 (variation of the excitation frequency for a fixed amplitude $Z_0 = 3.5$ cm). The wave amplitude displays hysteresis according to the path indicated by the arrows, □, decreasing excitation frequency (i.e. increasing Δ), △, increasing frequency. The theoretical amplitude, obtained from (3.8) and (3.9), is indicated by solid lines (calculated for $Q = 0$, but dissipation would change it only by a few per cent).

represented in figure 4(*a*), showing the amplitude versus time, obtained from a video record. We have compared the results with the growth rate predicted by (3.4), using the friction Q measured from the free decay of figure 4(*b*), and the optimal phase $\phi = \frac{1}{4}\pi$ (corresponding to the fastest growing instability). The agreement with theory is good only at moderate amplitude. At low amplitude, we observe a smaller growth rate (but the amplitude is then close to the experimental precision 0.5 mm). At high amplitude, the instability saturates by nonlinear effects, in a way similar to the case of a damped pendulum, shown by the solid curve on the left-hand side of figure 3(*b*).

The amplitude measured in the permanent regime resulting from the instability has been compared with the theoretical result (3.8) for the equivalent amplitude $|A|$ given by (3.9). In figure 6, this amplitude is represented versus the frequency misfit Δ for a given forcing amplitude Z_0 (along the line marked by arrows in figure 5). The amplitude appears to be lower than the predicted one, probably because of nonlinear dissipation effects. However, the general behaviour is qualitatively in agreement with the nonlinear theory; the transition is supercritical for negative Δ, and subcritical for positive Δ. The hysteresis for positive Δ is clearly observed in figure 6 by comparison between the results for increasing and decreasing frequencies (as indicated by arrows).

A form of nonlinear dissipation is the excitation of ripples at the interface, and even foam at large amplitude, that we observe in the central zone, with maximum shear. This can be simply explained as a consequence of shear instability, owing to the velocity difference $U_1 - U_2$ across the fluid interface. Instability is expected for $(U_1 - U_2)^2 > 2\ (1/\rho_1 + 1/\rho_2)\ [g\gamma(\rho_1 - \rho_2)]^{1/2}$ (see e.g. Lamb 1932, §268). This threshold corresponds to $U_1 - U_2 = 11$ cm s^{-1} in our experiments. The maximum velocity difference is related to the amplitude η_m of the vertical interface displacement by $U_1 - U_2 = 2\omega\eta_m$ (for a deep-water wave). In the case of the mode $n = 1$, with natural frequency $\omega = 3.55$ s^{-1}, this yields a threshold amplitude $\eta_m = 1.6$ cm for the onset of the secondary instability, inducing nonlinear dissipative effects for the primary mode.

As already mentioned, our results with interfacial waves are similar to the ones by Kalinichenko (1986), also performed with a kerosene–water interface. He found instability tongues at a frequency of 4–5% lower than theory, unlike ours, which may be due to his narrower tank (horizontal cross-section 40×500 mm^2). By contrast with our results, he found a free wave decay and instability threshold in good agreement with the prediction (4.2). Again, the difference may be due to his narrower geometry,

in which the interfacial friction is dominated by friction over the vertical walls. While (4.2) is appropriate for usual boundary-layer friction, the interfacial friction is probably more complex owing to some capillary effects. As in our experiments, the nonlinear behaviour is qualitatively in agreement with theory, but with a lower amplitude for the instability saturation, suggesting the presence of nonlinear dissipative effects.

5. Parametric instability for the continuous stratification

5.1. *The linear modes*

In a continuously stratified fluid, prepared with a density profile at rest $\tilde{\rho}(z)$ (decreasing with altitude z), a vertically displaced fluid particle receives a restoring force, leading to oscillation at the Brunt–Väisälä frequency N,

$$N = \left(-\frac{g}{\tilde{\rho}} \frac{\mathrm{d}\rho}{\mathrm{d}z} \right)^{1/2}. \tag{5.1}$$

The eigenmodes of oscillation have a simple explicit expression in the case of a uniform value of N, obtained for an exponential density profile $\tilde{\rho} = \rho_S \exp(-z/H')$. We can then calculate the oscillation modes by linearizing the inviscid fluid equations without any other approximation. In the case of small density differences, i.e. $H' \quad H$, the expressions simplify, and can be obtained by linearizing the Boussinesq equation. In our experiments, we have chosen the parameter $H' = 2.55$ m, so that $N = 1.96\ \mathrm{s}^{-1}$. The density difference between top and bottom is then 10%, so the Boussinesq approximation is not excellent, and we have calculated the exact results for linear modes with an exponential density profile.

The eigenmodes then have velocity components (u, v, w) and density fluctuation ρ' of the form (see Turner 1979)

$$\left.\begin{aligned} u &= -\dot{\eta}(t) \frac{q_x q_z}{q_x^2 + q_y^2} \sin q_x x \cos q_y y \left[\cos q_z z + \frac{\sin q_z z}{2 q_z H'} \right] \exp \frac{z}{2H'}, \\ w &= -\dot{\eta}(t) \cos q_x x \cos q_y y \sin q_z z \exp \frac{z}{2H'}, \\ \rho'/\tilde{\rho} &= (N^2/g)\, \eta(t) \cos q_x x \cos q_y y \sin q_z z \exp \frac{z}{2H'}. \end{aligned}\right\} \tag{5.2}$$

(The velocity component v along y is obtained by permuting x and y in the expression of u.) The impermeability boundary conditions impose that the three components of the wavenumber vector $\boldsymbol{q}$ are quantified

$$q_x = n\pi/L, \quad q_y = m\pi/W, \quad q_z = p\pi/H. \tag{5.3}$$

It will be useful to define the modulus q by $q^2 = q_x^2 + q_y^2 + q_z^2$, and the angle θ of the wave number vector with the horizontal, such that $\sin\theta = q_z/q$. The Boussinesq results are obtained from the expressions (5.2) by suppressing all terms involving H'. The standing modes are then expressed as a superposition of four propagating waves with the same wavenumber q, and with the angles θ and $-\theta$ with the horizontal.

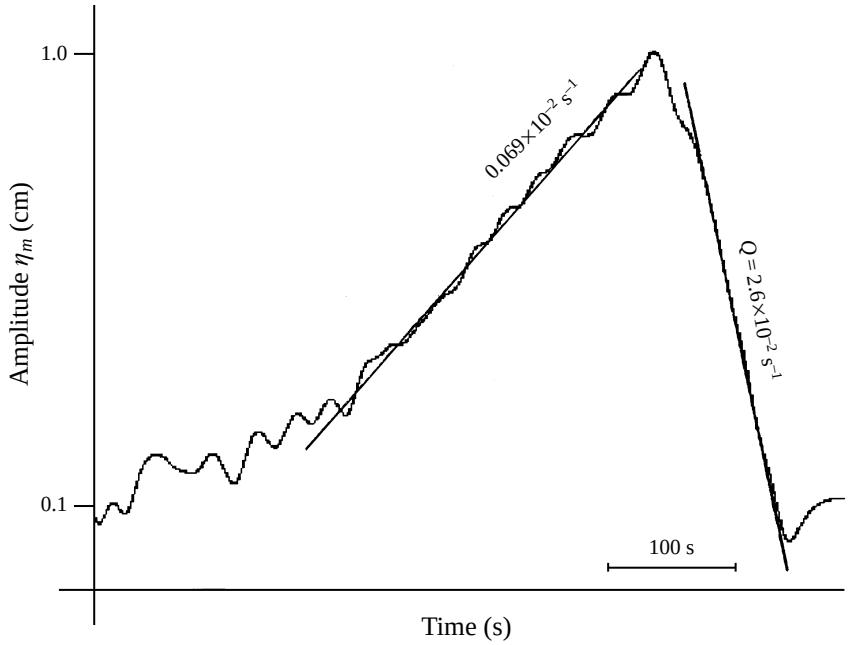

FIGURE 7. Amplitude of a continuously stratified mode (1, 0, 1) function of time, in lin-log coordinates, showing the exponential amplification (excitation frequency 0.432 Hz and amplitude $Z_0 = 11$ cm), followed by free exponential decay, after stopping the excitation. The amplitude is extracted from the probe signal by the filtering (2.1).

Mode	(1, 0, 1)	(2, 0, 1)	(4, 0, 2)	(3, 0, 2)
Q_{calc} (s^{-1})	1.4×10^{-2}	1.0×10^{-2}	1.1×10^{-2}	1.25×10^{-2}
Q (s^{-1})	2.6×10^{-2}	1.6×10^{-2}	1.4×10^{-2}	1.6×10^{-2}
Q_{bulk}/Q_{bound} (%)	1	4	16	8

TABLE 2. Decay rate Q_{calc} for modes with a uniform stratification, calculated from (5.5), compared to the measured rate Q; the ratio Q_{bulk}/Q_{bound} is also given.

The mode amplitude is characterized by the maximum vertical displacement $\eta(t)$, which oscillates with the natural frequency

$$\omega = N\cos\theta. \tag{5.4}$$

This expression corresponds to the Boussinesq approximation, but the exact relation for the exponential profile brings only a relative correction smaller than 0.3×10^{-3} with our experimental conditions.

5.2. *Energy dissipation*

Energy dissipation is the sum of a boundary-layer term Q_{bound} and a bulk term Q_{bulk}, which is generally much smaller (of course there is no interfacial dissipation). The boundary layers for the horizontal velocity have the same structure as in a fluid with uniform density, but the boundary layers for the vertical velocity are directly influenced by buoyancy effects, and are calculated by McEwan (1971). The resulting dissipation

coefficients are obtained as a direct generalization of McEwan's results (including three-dimensional and non-Boussinesq effects),

$$\left.\begin{aligned} Q_{bulk} &= \tfrac{1}{2}\nu q^2, \\ Q_{bound} &= (\omega\nu/2)^{1/2}\sin^2\theta\left\{(2-\delta(q_x))\frac{\cot\theta+q_y^2/q_h^2}{L}+(2-\delta(q_y))\frac{\cot\theta+q_x^2/q_h^2}{W}\right. \\ &\qquad \left.+s\frac{\sin^2\theta}{H}\left(1-\frac{H}{2H'}\right)\right\}, \end{aligned}\right\} \quad (5.5)$$

where $\delta(q) = 1$ if $q = 0$ and $\delta(q) = 0$ if $q \neq 0$, $s = 1$ when the upper surface is free, and $s = 2$ when it is rigid. Even when we have a free surface, its tangential motion is generally frozen by a thin film of impurities, so we always choose $s = 2$ (dissipation is dominated by the vertical lateral walls, so this choice is not essential). The term q_h denotes the modulus of the horizontal wave number projection, defined by $q_h^2 = q_x^2 + q_y^2$. We have approximated the small non-Boussinesq correction to the lowest order (by the term in H/H'). Note that the boundary dissipation Q_{bound} depends only on the direction of the wavenumber vector, not its modulus. For the two-dimensional modes that we are studying here ($q_y = 0$), Q_{bound} depends only on the angle θ, like frequency. By contrast, the bulk dissipation Q_{bulk} depends on the wavelength, but it is much smaller than Q_{bound} for the typical waves that we excite. Some dissipation of potential energy by diffusion of concentration is also expected, but this is negligible here owing to the low salt diffusivity in comparison with viscosity.

We have experimentally checked the dissipation rate (5.5) in the free decay of different modes. We characterize this decay by the amplitude of the probe signal, extracting the envelope of the oscillation by the filtering procedure (2.1). We first excite the mode by parametric instability, and stop the forcing to observe the free decay, as shown in figure 7. The measured decay rate is of the correct order of magnitude, but always faster than the theoretical prediction, as shown in table 2. McEwan (1971) made similar comparisons for decaying waves initially generated by a wavemaker, and found a better agreement with (5.5). We do not have a clear explanation for the greater discrepancy in our experiment. We notice that in our case, the boundary layers involving a vertical velocity play a dominant role in the dissipation, in contrast to McEwan's experiments. This boundary layer produces steep horizontal density gradients near the walls, and should be unstable even for a small wave amplitude, according to Robinson & McEwan (1975).

Indeed, these authors experimentally found that the boundary layer near a vertically oscillating wall with velocity amplitude w is unstable for $w > 7\ (2\omega\nu)^{1/2}$, in the range $0.7 < \omega/N < 1$ corresponding to our experiments. This threshold velocity is $w = 1.2$ cm s^{-1} in our experiments, and is achieved for an amplitude of vertical displacement $\eta_m = w/\omega = 0.85$ cm. In practice, this value is attained in most of our experimental runs (for instance in figure 7), so we expect discrepancies with the laminar wall friction law. Notice that in a non-stratified fluid, the instability threshold is much higher, $w \approx 250\ (2\omega\nu)^{1/2} = 43$ cm s^{-1}, and we expect this threshold to be valid also in the stratified case for boundary layers with horizontal velocity.

5.3. *Parametric instability*

As in the interfacial case, we always excite modes with a natural frequency of half the frequency of the platform. However, the modes are not isolated; whatever the excitation frequency (for $\omega_e < 2N$), we excite some mode for a sufficiently high forcing.

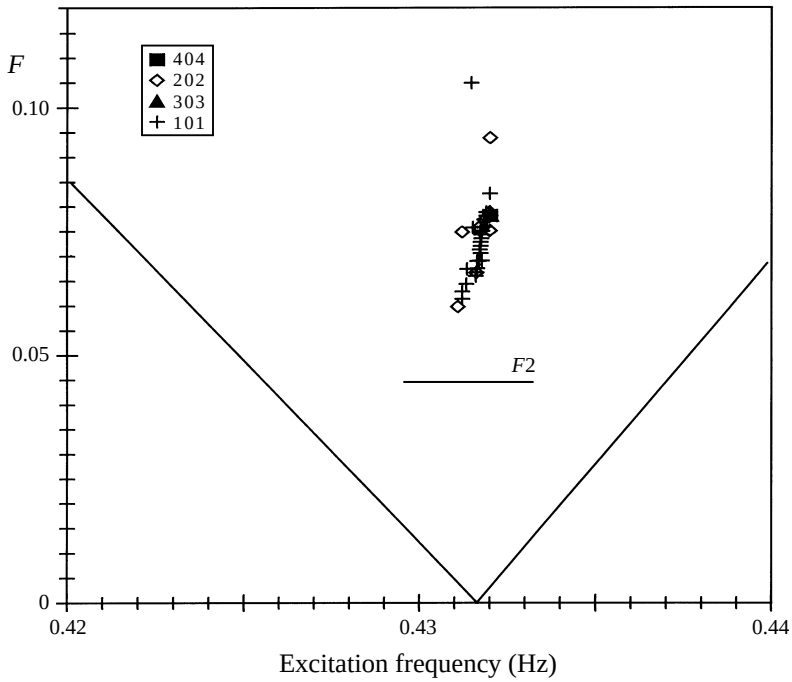

FIGURE 8. Instability diagram in the continuously stratified case, indicating parameters for which different modes $(n, 0, n)$ have been observed, as specified by the labels. The different harmonics (visualized in figure 9) can be excited in an intricate way for the same experimental parameters. The theoretical inviscid instability tongue, common to all these modes, is indicated by the solid line, as well as the threshold $F2$ (obtained with the measured decay rate $Q = 2.6 \times 10^{-2}\ \mathrm{s}^{-1}$). We have limited the exploration to $\Delta \approx 0$, otherwise different modes appear in a non-reproducible way, so the experimental edge of the instability tongue is not well defined.

This is easily understood from the dispersion relation (5.4); for any frequency $\omega_e < 2N$, the wavevectors with angle $\theta = \arccos(\omega_e/2N)$ can be excited. The possible values of θ are constrained by the quantization condition (5.3), but this restriction is not severe for high wavenumbers, and in practice one or several modes, two-dimensional or three-dimensional, can be excited for any excitation frequency $\omega_e < 2N$. For $\omega_e > 2N = 3.9\ \mathrm{s}^{-1}$, we do not observe any internal wave excitation, as expected. For the much higher frequency $\omega_e = 2\,(g\pi/L)^{1/2} = 21.8\ \mathrm{s}^{-1}$, we excite the first free-surface mode. By contrast the free surface remains unperturbed in the range of internal wave excitation $\omega_e < 2N$ in which we are interested here.

The tongues of parametric instability for the different modes intersect in an intricate way, and it is not possible to study isolated tongues as in the interfacial case (as in figure 5). In practice, the selection of a mode is very sensitive to the frequency and amplitude of forcing, and even sometimes to the initial perturbation. Three-dimensional modes are commonly obtained, and are often in competition with a two-dimensional mode, as we move away from the centre of its instability tongue. The outcome of various experiments is given in figure 8, for the excitation frequency of the fundamental mode (1, 0, 1), and its different harmonics $(n, 0, n)$, which have the same frequency $N/\sqrt{2}$. As we move away from the tongue centre (i.e. $\Delta \neq 0$), other modes dominate, in a non-reproducible way (depending on initial disturbances), and we were not able to explore the lateral limits of the instability tongue. Visualizations of the

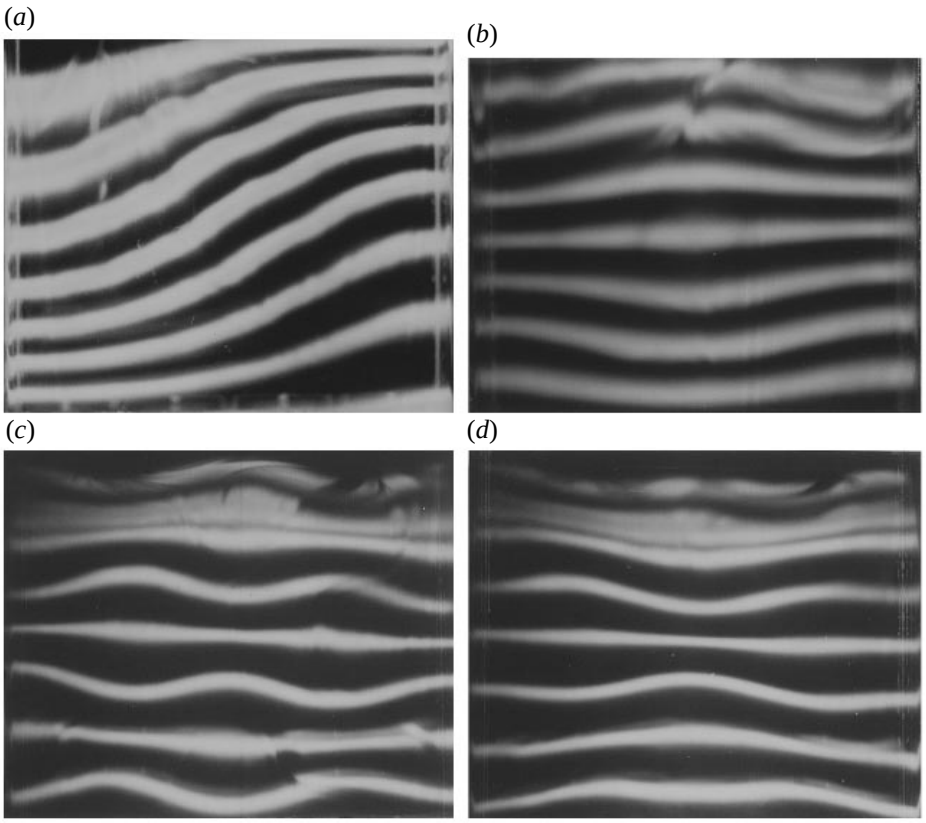

FIGURE 9. Different modes obtained for the same experimental parameters $f_e = 0.432$ Hz and amplitude $Z = 10.5$ cm. The views are taken during the growth of the primary instability and the deformation fields are smooth (but some dye bands have been initially perturbed or broken by air bubbles as the tank was filled). (*a*) mode (1, 0, 1), (*b*) mode (2, 0, 2), (*c*) mode (4, 0, 4), (*d*) superposition of (2, 0, 2) and (4, 0, 4).

different harmonics are represented in figure 9. We can also observe a superposition of two modes as in figure 9(*d*). As stated in § 5.2, energy dissipation is dominated by the boundary effect Q_{bound}, which is the same for all the harmonics (n, 0, n). Therefore we expect that the threshold of instability is also the same for the first harmonics, and this is in agreement with observations. However, this common threshold is somewhat higher than the theoretical prediction, represented by the horizontal line in figure 8.

To expand this point, we have measured the growth rate of the parametric instability (figure 10(*a*)), and compare it with the prediction $s - Q$, with Q given by (5.5), represented by the solid line. The growth rate is lower than theory, consistently with the stronger decay of the free mode. The growth rate is, however, higher than the prediction for instability using the measured decay rate (dashed line). We think these effects are due to changes of the wall friction associated with perturbations of the boundary layers along the vertical walls, and further studies would be needed to clarify these effects.

5.4. *Nonlinear behaviour of the parametric instability*

We can predict the saturation amplitude, combining (3.10) and (3.8), with a misfit $\Delta = 0$ (indeed we only observe growth at the centre of the instability tongues). This

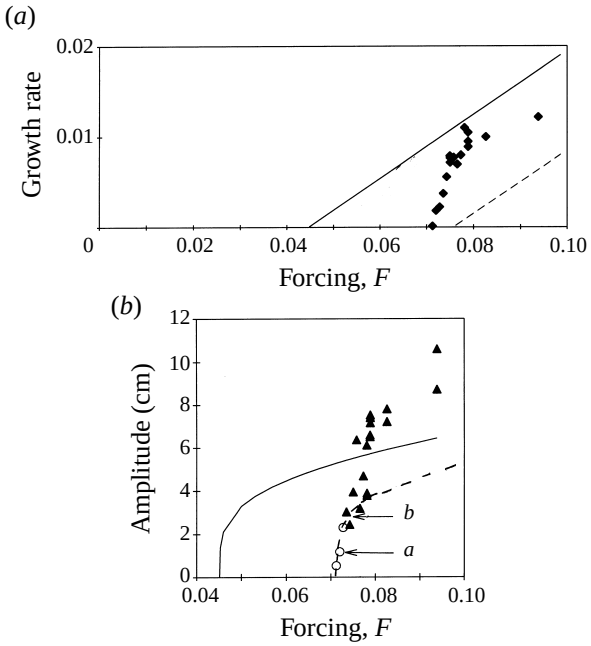

FIGURE 10. (*a*) Growth rate of the mode (1, 0, 1) versus the forcing parameter F. The experimental points are between the solid and dashed theoretical lines, respectively, obtained with the theoretical decay rate (5.5), and with the decay rate $Q = 2.63 \times 10^{-2}\ \mathrm{s}^{-1}$ measured in figure 7. (*b*) Maximal amplitude reached by the growing mode (1, 0, 1) compared with the two theoretical estimates as in (*a*). ○, pure oscillation, ▲, presence of the subharmonic perturbation. The points labelled *a* and *b* correspond to the signals shown in figure 11.

saturation amplitude, supposedly obtained at large times, is close to the maximum amplitude of the wave reached at the end of its growth, as shown by the solid line in the left side of figure 3(*b*). In figure 10(*b*), we compare this prediction (solid line) with the maximum amplitude measured in the experiment. For forcing close to the threshold, the maximum amplitude is lower than predicted, and this reflects the lower growth rate shown in figure 10(*a*). The saturation amplitude predicted by introducing the measured decay rate Q in (3.8) is by contrast too low (dashed line), and this is also consistent with the results on the growth rates. For larger forcing, the maximum amplitude becomes higher than theoretical predictions, pointing out limitations of the weakly nonlinear single mode model leading to (3.10).

Very close to the instability threshold (open circles in figure 10), the primary wave slowly grows and saturates in a steady regime, as expected from the model of an isolated mode. This results in a periodic signal, as shown in figure 11(*a*). In generic instability problems, the linearly unstable modes interact together in the weakly nonlinear regime appearing slightly beyond the instability threshold. Therefore we would expect in our case an interaction between the different harmonics (n, 0, n). Depending on the coupling constants, such interactions lead to steady regimes, involving either an isolated instability mode, or a superposition of them, or lead to time-dependent regimes. Our results indicate that the excited modes tend to remain separate, which would correspond to the first possibility. Notice, however, that internal waves interact efficiently only when they form a resonant triad, involving three modes

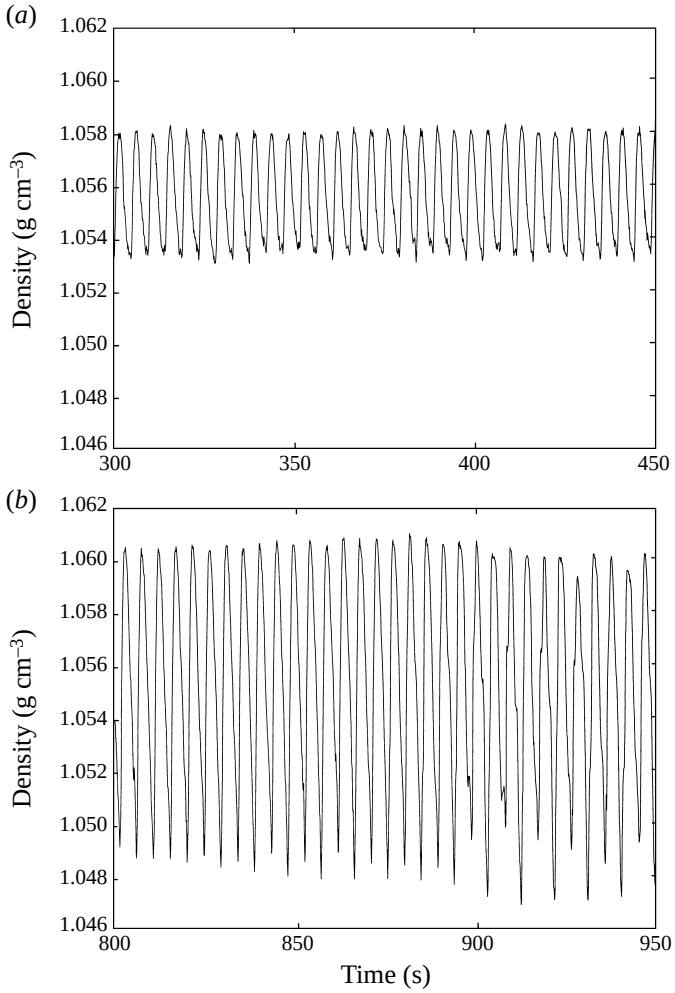

FIGURE 11. Probe signal showing the saturation of the primary instability, for mode (1, 0, 1) (the probe is at height $z = 0.45\,H$, at a distance $x = \frac{1}{5}L$ from the wall). (*a*) Saturation into a permanent oscillation, very close to the threshold, corresponding to label *a* in figure 10(*b*). (*b*) Growth of a subharmonic secondary instability, seen as a modulation of the oscillation, for a higher primary wave amplitude (label (*b*) in figure 10(*b*)).

with respective wavevectors $\boldsymbol{k}_1$, $\boldsymbol{k}_2$, $\boldsymbol{k}_3$ satisfying $\boldsymbol{k}_3 = \boldsymbol{k}_1 \pm \boldsymbol{k}_2$ and frequencies ω_1, ω_2, ω_3 satisfying $\omega_3 = \omega_1 \pm \omega_2$. The latter condition cannot be satisfied for three waves excited by the primary instability, as they have the same frequency $\frac{1}{2}\omega_e$. Therefore, the interaction between the different primary waves is very weak near their instability threshold.

The regime of an isolated standing wave is obtained only very close to the instability threshold. When the primary wave exceeds the amplitude $\eta \approx 2$ cm (triangles in figure 10), a secondary instability appears: a secondary wave grows with half the frequency of the primary wave. The growth of this subharmonic perturbation can be seen directly as a modulation of the primary oscillation in the probe signal of figure 11(*b*). In the next section we analyse the structure of this secondary instability, as well as the subsequent dynamics.

6. Secondary instability and turbulent behaviour in the continuously stratified case

6.1. *Secondary instability and wave-breaking*

The spatial structure of the secondary instability is visualized in figure 12(*b*). It is a plane wave packet developing at the node (in displacement) of the primary wave. This instability has been theoretically investigated from two points of view. According to McEwan & Robinson (1975), the secondary wave is transported by the primary wave oscillation, resulting in a modulation of its wave-vector angle with respect to the horizontal, and a corresponding modulation of its natural frequency (5.4), leading to parametric instability. The same parametric instability can be also viewed as a particular case of resonant wave interaction among a triad made of the primary wave and two secondary waves (McEwan 1971). The maximum growth rate is obtained in the limit of large secondary wavenumbers (in the absence of viscosity), with a frequency of half the primary wave frequency.

Bouruet-Aubertot *et al.* (1995) have shown by direct numerical computations that this mechanism of parametric instability indeed initiates the instability of a standing wave (with sufficiently high frequency). A remarkable spatial organization into a wave packet was shown, very similar to the experimental observation of figure 12(*b*). The phase of the secondary wave is locked with respect to the primary wave, corresponding to an optimal amplification by parametric instability (figure 4 of Bouruet-Aubertot *et al.* (1995). The same phase locking is observed in the laboratory experiments.

The growth rate of the secondary instability was found to be in good numerical agreement with the theory of resonant interactions. For the primary wave (1, 0, 1), the predicted growth rate, from equation (5.14) of Bouruet-Aubertot *et al.* (1995), is $s_q = 0.098\, k_x^2 a$, where k_x is the wavenumber along the horizontal direction, and a the primary wave amplitude in stream function. This amplitude is related to the vertical displacement η_m by $a = \omega\eta_m/k_x$, so that $s_q = 0.098\, k_x \eta_m \omega$. Taking $k_x = \pi/L = 0.12\ \mathrm{cm}^{-1}$, and $\omega = 1.36\ \mathrm{s}^{-1}$, this yields an inviscid growth rate $s_q = 0.43\ \eta_m/L$. The wavenumber of the perturbation is about $q \approx 2\ \mathrm{cm}^{-1}$, and the friction, calculated from (5.5), is $3.3 \times 10^{-2}\ \mathrm{s}^{-1}$. Equating this rate with s_q yields a threshold $\eta_m = 1.9$ cm, in reasonable agreement with our observations reported in figure 10. In most of our experiments, the primary wave exceeds this amplitude, and the secondary instability is indeed observed.

The secondary wave packet has a structure close to a plane wave, for which nonlinear effects vanish, whatever the amplitude. As a consequence, there is no saturation of the secondary instability, until local density overturning occurs, and new instabilities rapidly lead to the onset of turbulence. The presence of a strong shear and unstable vertical density gradient both foster these instabilities. Visualizations in the plane of the primary wave show typical structures of shear instability (figure 12(*c*), left-hand side), while rolls or mushrooms are detected in the transverse plane (figure 12(*c*), right-hand side).

These observations are consistent with a Floquet stability analysis for infinitesimal perturbations on a plane wave (Klostermeyer 1991). A plane wave with moderate amplitude is found to be unstable by parametric instability, corresponding to resonant interaction within a wavenumber triad in the vertical plane, and this is analogous to our result for the instability of the standing wave. By contrast, three-dimensional modes are found to be the most unstable when the wave amplitude is so large that density overturning occurs, and this is the case for our secondary wave. Notice that the observed organization of the instability into transverse rolls is commonly observed in

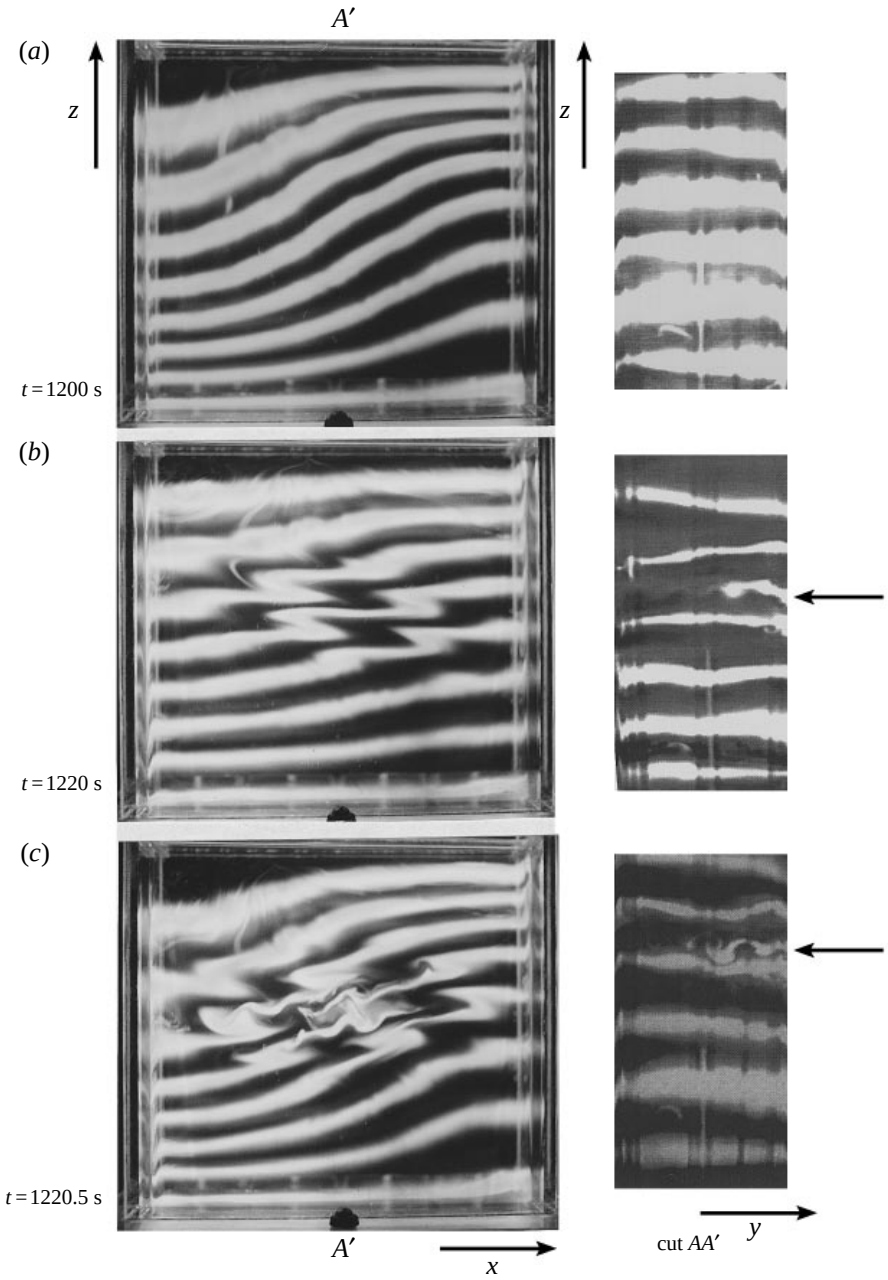

FIGURE 12. Visualization of the wave breaking, face view (left), and side view (right) with the laser sheet turned by 90°, along the lines AA' (excitation frequency 0.432 Hz and amplitude $Z_0 = 11$ cm). The time elapsed from the beginning of the experiment is indicated for the side view. (The correspondence with the face view is only approximate, as it corresponds to a different experimental run.) (*a*) The growing primary mode (1, 0, 1). (*b*) A secondary wave packet growing by parametric instability. In the side view a dye strip is doubled by overturning, and a convective instability begins to grow in the region of overturning (arrow). (*c*) The wave has broken into a small-scale instability, and the development of convective mushrooms is visible on the side view.

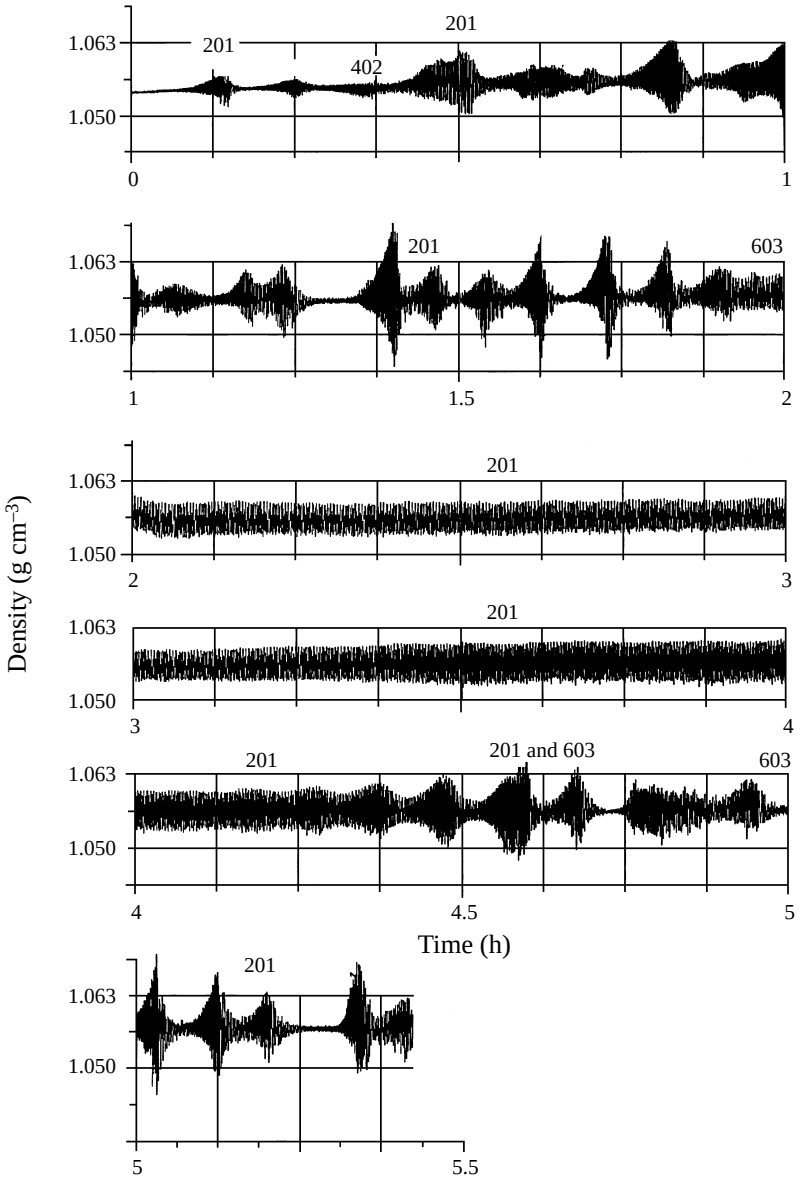

FIGURE 13. Long time record of the probe signal (successive pieces), showing intermittent and regular phases. The observed spatial structures are indicated by their wavenumber vectors (n, m, p). Amplitude of excitation $Z_0 = 4.5$ cm, frequency $f_e = 0.560$ Hz, probe position $z = 0.45\,H$, $x = \frac{1}{2}L$.

the presence of shear and/or convective instability. It has been carefully analysed by Schowalter, Van Atta and Lasheras (1994) in the case of a stratified shear layer.

6.2. *Intermittent regimes*

The development of the secondary instability and breaking reacts on the primary wave, whose amplitude decays, until a new growth is observed, leading to a remarkable intermittent behaviour, see figure 13. Different harmonics (n, 0, n) with the same natural frequency often grow alternatively. Phases of well-established, although chaotic, wave amplitude are also observed, so that the intermittence is intermittent.

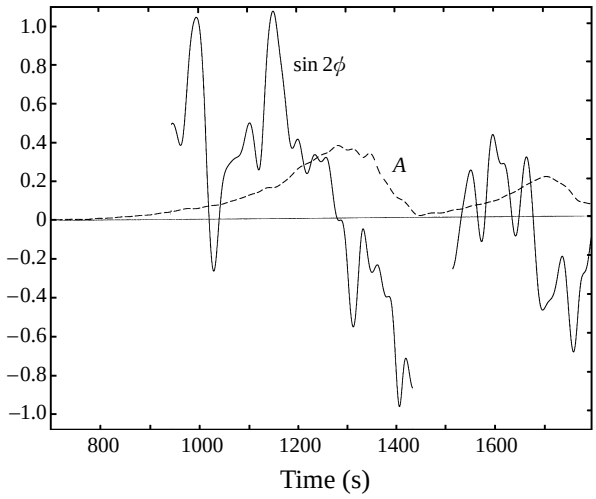

FIGURE 14. Primary wave amplitude A (dashed line) and phase ϕ versus time, obtained from the probe signal by (2.1). We have represented $\sin 2\phi$ (solid line), which represents the energy input by the forcing, according to (3.4). The phase is interrupted when the amplitude is too small ($\frac{1}{10}$ of its maximum) to obtain a reliable result. We observe that the primary wave is growing when $\sin(2\phi) > 0$ and decreasing when $\sin(2\phi) < 0$, in agreement with (3.4) (mode (2, 0, 1), $f_e = 0.560$ Hz, $Z_0 = 4$ cm, probe position $z = 0.45H$, $x = \frac{1}{2}L$).

Flow visualization indicates that intermittence corresponds to a global change of the wave amplitude, and is not limited to the probe signal at a given position. Notice that the changes of modes are not due to a change of natural frequencies, associated with a progressive mixing of the basic density profile by wave breaking. This mixing is very slow, and the basic density profile remains within 1 % during a full working day. We see in figure 13 that the same sequence, for instance the growth of the pure (2, 0, 1) mode occurs again at the same excitation frequency after several hours.

Although this complex nonlinear behaviour is clearly outside the scope of a single oscillator model, it is reminiscent of the model (3.7) with a small relative dissipation Q/s (figure 2(*a*)). As the wave amplitude increases, the wave oscillation lags, and the phase ϕ corresponds to a negative forcing and wave decay, until a new growth occurs, and so on in a cyclic way. However, this modulation of the amplitude is damped by the dissipation (as in figure 2(*b*)), and should disappear as we are close to the threshold $Q/s \approx 1$. It seems that mode interactions excite this amplitude modulation against viscous damping. This interpretation is confirmed by time series of the primary wave amplitude $A(t)$ and phase $\phi(t)$, obtained by (2.1), represented, respectively, by a dashed line and a solid line in figure 14. We have plotted $\sin 2\phi$, directly related to the energy input by (3.4). We observe that $\sin 2\phi$ is predominantly positive during phases of growth, corresponding to energy input, and negative during decay, corresponding to a negative forcing. (Notice that the phase ϕ obtained from the probe is perturbed by the probe wake, as indicated in §2 (we should have $\sin 2\phi = 1$ during the initial growth). However, it still proves a good indication for the sign of $\sin 2\phi$, as shown by comparison with image analysis during the initial growth of the primary wave.) Therefore, the secondary instability influences the primary wave both by draining its energy and by changing its phase, both effects favouring the observed intermittent behaviour.

Further characterization of the intermittent behaviour is provided by spectral analysis (figure 15). The time spectrum is dominated by the primary wave frequency

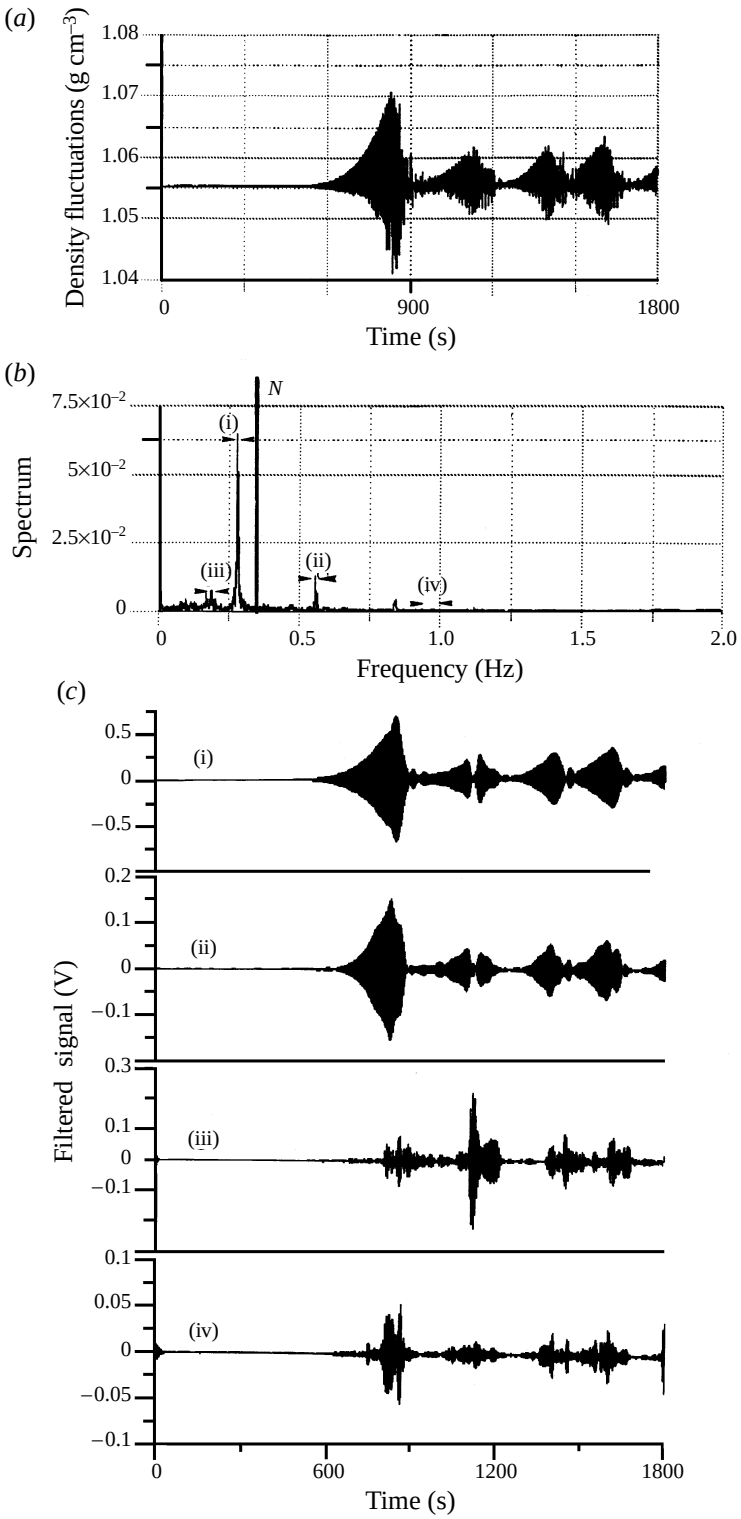

FIGURE 15. (*a*) Probe signal (*b*), time spectrum, and (*c*) band pass filtered signal. Mode (2, 0, 1) is dominant and the probe is at location ($x = \frac{1}{2}L$, $z = 0.45\ H$). In (*c*), the signal is filtered in the different

and its harmonics, as well as other secondary peaks, and a continuous background. We have filtered the signal around these different frequencies. The first harmonics follows the primary wave. It behaves like the square of the primary wave amplitude. By contrast, other frequencies are mainly excited during breaking of the primary wave, i.e. when its amplitude decreases. The secondary peaks, other than harmonics, must be excited by resonant interaction with the primary wave. Although a subharmonic wave is first excited, as discussed above, other frequencies appear later in time as some disorder sets in the wave field. The selection of these secondary frequencies slowly changes with time, and we cannot clearly characterize them. However, we observe that they are always below the primary wave frequency. This is in agreement with a general rule for a wave instability by resonant interaction. The growing perturbing waves must have a frequency lower than the primary wave (Davis & Acrivos 1967; Hasselmann 1967).

A continuous spectrum at frequencies larger than N is also excited, mainly during breaking. These frequencies are beyond the range of internal waves, and must be interpreted as the result of the advection of fine scale structures. For sufficiently high forcing, this continuous spectrum depends on frequency with a ω^{-3} law, as shown by Benielli and Sommeria 1996). This result has been interpreted as a k^{-3} spatial spectrum of compliant waves, transported across the fixed probe by the large-scale internal waves.

7. Conclusions

We have investigated the parametric excitation of internal waves in two different cases, with a density interface, and with a continuously stratified case. Our experiments with a density interface basically reproduce previous work by Kalinichenko (1986), and are presented here mostly as a reference case to compare with the new results obtained in the continuously stratified case.

The interfacial waves behave like surface gravity waves. Modes are isolated and well separated, so that each mode is like a pendulum, with amplitude specified by (3.9). The instability occurs in tongues in the space (F, ω_e), and grows until a steady regime is obtained. The instability is subcritical on the left-hand side (low ω) and supercritical on the right-hand side (high ω) of each tongue, in agreement with theory.

However, friction effects are not well understood. The friction is calculated using a boundary-layer approximation, but the observed decay rate is about 50 % higher than expected from this calculation. Given this higher friction, the instability threshold and the initial growth rate are in agreement with the theory of parametric instability. The level of saturation in the permanent regime is lower than theory, even with the friction deduced from wave decay. Nonlinear dissipative effects must therefore take place, probably by excitation of capillary waves at the interface. We indeed observe the development of ripples by shear instability, but hysteresis of wetting at the wall may be a further source of energy dissipation. Kalinichenko (1986) found friction in better agreement with theory, but a small discrepancy in the wave frequency. These differences may be due to their smaller interfacial area in comparison with wall area, as discussed in §4.

---

frequency intervals indicated by the labels in the spectrum (*b*). The signal is dominated by the primary wave amplitude (i). Its harmonic (ii) behaves similarly. The lower-frequency component (iii) and the high-frequency one (iv) burst during wave-breaking events, while the primary wave-amplitude decays. This observation suggests an energy transfer from the primary wave to other modes during breaking events.

In the case of a uniform stratification, the instability tongues of different modes strongly overlap, in contrast with the interfacial case. Indeed the harmonics (n, 0, n) have the same frequency, and the same damping rate by viscous friction in the boundary layer (dominating the dissipation), resulting in the same instability tongues. Competition with three-dimensional modes is also observed. It was therefore not possible to clearly identify instability tongues.

The different modes are excited at the expected frequency, but their damping is stronger than predicted by (5.5), using the boundary-layer theory. By contrast, McEwan (1971) found good agreement with the same theory. In our geometry, boundary layers involving the vertical velocity component play a dominant role in energy dissipation, in contrast to McEwan's experiments. In contrast to the case of horizontal velocity, these boundary layers induce steep horizontal density gradients, which are the cause of specific instabilities, probably increasing friction. More experiments on boundary-layer friction would be needed to clarify this point.

The instability threshold is higher than theory, but in good agreement when the friction obtained from the decay rate is introduced in the theory of parametric instability. Beyond the threshold, the growth is between these two predictions, which would mean that friction decreases when the wave is growing in amplitude. The saturation amplitude is also higher than the theoretical prediction using the observed friction.

Although the instability tongues for the different harmonics (n, 0, n) are nearly identical, we observe that each mode can grow with few interactions with each other. Indeed, the coupling between these modes is weak, as they are not in resonant interaction.

By contrast, secondary instabilities and breaking of the primary wave play an essential role in the dynamics. The instability of the standing wave excites a well-organized secondary wave packet in the vertical plane, with a frequency of half the primary wave frequency. This secondary wave reaches high amplitude, with strong shear and local density over-turning, and rapid three-dimensional instabilities lead to the onset of turbulence. This mechanism of breaking was theoretically proposed by McEwan (1971) and McEwan & Robinson (1975), and simulated by the two-dimensional computations of Bouruet-Aubertot *et al.* (1995), but not clearly obtained in previous laboratory experiments. The modes (1, 0, 1) and (2, 0, 1) that we have investigated systematically break through this process. We did not study modes with lower frequency (it would require a larger amplitude for the oscillating platform), which develop other instabilities, as shown by the computations of Bouruet-Aubertot *et al.* (1995) and the laboratory experiments of Taylor (1992) or Thorpe (1994).

The secondary instability and breaking react on the primary wave by decreasing its energy, and changing its phase. Both effects contribute to a decay of the primary wave after breaking, followed by a new phase of growth. This mechanism is reminiscent of a parametrically excited pendulum (figure 3*a*), but it is here excited against friction by the secondary instabilities. A remarkable intermittent behaviour over long timescales results. We observe phases with a well-organized growing wave, and phases with a more complex, decaying, field, including small-scale turbulence and low-frequency modes excited by resonant wave interactions.

Our analysis may find applications for other kinds of waves, such as inertial waves occurring in a rotating fluid. Inertial waves are excited by a form of parametric instability in a vortex with uniform vorticity and elliptical streamlines (the oscillating strain modulates the angle of the wave vector with respect to the axis of rotation, thus modulating the natural frequency of the inertial wave). A laboratory experiment by

Malkus (1989) indicates that this instability occurs in an intermittent way. This may be due to the development of secondary instabilities initiated by resonant interactions, as in our experiment.

REFERENCES

Benielli, D. & Sommeria, J. 1996 Excitation of internal waves and stratified turbulence by parametric instability. *Dyn. Atmos. Oceans* **23**, 335–343.

Bouruet-Aubertot, P., Sommeria, J. & Staquet, C. 1995 Breaking of standing internal gravity waves through two-dimensional instabilities. *J. Fluid Mech.* **285**, 265–301.

Bouruet-Aubertot, P., Sommeria, J. & Staquet, C. 1996 Stratified turbulence produced by internal wave breaking. *Dyn. Atmos. Oceans* **23**, 357–369.

Davis, R. E. & Acrivos, A. 1967 The stability of oscillatory internal waves. *J. Fluid Mech.* **30**, 723–736.

Drazin, P. G. 1977 On the instability of an internal gravity wave. *Proc. R. Soc. Lond.* A **356**, 411–432.

Faraday, M. 1831 On a peculiar class of acoustical figures; and on certain forms assumed by groups of particles upon vibrating elastic surfaces. *Phil. Trans. R. Soc. Lond.* **121**, 299–340.

Harrison, W. J. 1908 *Proc. Lond. Math. Soc.* (2) **6**, 396.

Hasselmann, K. 1967 A criterion for nonlinear wave stability. *J. Fluid Mech.* **30**, 737–739.

Kalinichenko, Y. A. 1986 Laboratory investigation of parametric instability in a two-layer fluid. *Izv. Acad. Sci. USSR Atmos. Ocean. Phys.* **22**, 155–158.

Kalinichenko, T. A., Sekerzh-Zen'kovich, S. Ya. & Timofeev, A. S. 1991 Experimental study of the velocity field of parametrically excited waves in a two-layer liquid. *Izv. Akad. Nauk SSSR Mekh. Zhid. i Gaza* **5**, 161–166.

Klostermeyer, J. 1991 Two and three-dimensional parametric instabilities in finite amplitude internal gravity waves. *Geophys. Astrophys. Fluid Dyn.* **61**, 1–25.

Lamb, H. 1932 *Hydrodynamics*. Dover.

Lombard, P. N. & Riley, J. J. 1996 On the breakdown into turbulence of propagating internal waves. *Dyn. Atmos. Oceans* **23**, 345–355.

Maas, L. R. M., Benielli, D., Sommeria, J. & Lam, F. P. A. 1997 Observation of an internal wave attractor in a confined, stably-stratified fluid. *Nature* **388**, 557–561.

McEwan, A. D. 1971 Degeneration of resonantly-excited standing internal gravity waves. *J. Fluid Mech.* **50**, 431–448.

McEwan, A. D. & Robinson, R. M. 1975 Parametric instability of internal waves. *J. Fluid Mech.* **67**, 667–687.

Malkus, W. V. R. 1989 An experimental study of global instabilities due to the tidal distortion of a rotating elastic cylinder. *Geophys. Astrophys. Fluid Dyn.* **48**, 123–134.

Meron, E. 1987 Parametric excitation of multimode dissipative systems. *Phys. Rev.* A **35**, 4892–4895.

Mied, R. P. 1976 The occurrence of parametric instabilities in finite amplitude internal gravity waves. *J. Fluid Mech.* **78**, 763–784.

Miles, J. W. 1967 Surface-wave damping in closed basins. *Proc. R. Soc. Lond.* A **297**, 459–475.

Miles, J. W. 1984 Nonlinear Faraday resonance. *J. Fluid Mech.* **146**, 285–302.

Miles, J. W. & Henderson, D. 1990 Parametrically forced surface waves. *Ann. Rev. Fluid Mech.* **22**, 143–165.

Muller, P., Holloway, G., Henyey, F. & Pomphrey, N. 1986 Non-linear interactions among internal gravity waves. *Rev. Geophys.* **24**, 493–536.

Nayfeh, A. H. 1973 *Perturbation Methods*. Wiley Interscience.

Robinson, R. M. & McEwan, A. D. 1975 Instability of a periodic boundary layer in a stratified fluid. *J. Fluid Mech.* **68**, 41–48.

Schowalter, D. G., Van Atta, C. W. & Lasheras, J. C. 1994 A study of streamwise vortex structure in a stratified shear layer. *J. Fluid Mech.* **281**, 247–291.

Sekerzh-Zen'kovitch, S. Ya. 1983*a* Parametric excitation of finite-amplitude waves at the interface of two liquids with different densities. *Dokl. Acad. Nauk SSSR* **272**, 1083–1086.

Sekerzh-Zen'kovitch, S. Ya. 1983*b* Parametric resonance in a stratified liquid in a container undergoing vertical vibrations. *Sov. Phys. Dokl.* **28**, 445–446.

Taylor, J. R. 1992 The energetics of breaking events in a resonantly forced internal wave field. *J. Fluid Mech.* **239**, 309–340.

Thorpe, S. A. 1968 On standing internal gravity waves of finite amplitude. *J. Fluid Mech.* **32**, 489–528.

Thorpe, S. A. 1994 Observations of parametric instability and breaking waves in an oscillating tilted tube. *J. Fluid Mech.* **261**, 33–45.

Thual, O., Douady, S. & Fauve, S. 1989 Parametric instabilities in *Instabilities and nonequilibrium structures II* (ed. R. Tirapegui & I. Villarroel), pp. 227–237. Kluwer.

Turner, J. S. 1979 *Buoyancy Effects in Fluids*. Cambridge University Press.